Article

Article

Template-free Synthesis of Mesoporous and Crystalline Transition Metal Oxide Nanoplates with Abundant Surface Defects

Mingzhen Hu,[1,2,6] Wenjuan Yang,[5,6] Haiyan Tan,[3] Lei Jin,[2] Lei Zhang,[1,2] Peter Kerns,[2] Yanliu Dang,[3] Shanka Dissanayake,[2] Samuel Schaefer,[3] Ben Liu,[1,*] Yuanyuan Zhu,[3,*] Steven L. Suib,[2,3,4,*] and Jie He[2,3,4,7,*]

SUMMARY

Mesoporous transition metal oxides with crystalline walls show promising applications in catalysis and energy storage. Syntheses of those crystalline mesoporous oxides, however, currently remain as an unmet challenge because of the large volume shrinkage during crystallization in a sol-gel process. Here, we demonstrate a facile and general template-free method to prepare six mesoporous transition metal oxides, e.g., CuO, CoO, and spinel MCo_2O_4 (M = Co, Cu, Mn, Zn), with highly crystalline walls and continuous mesopores in the forms of two-dimensional nanoplates or nanosheets. The method is based on the thermal crystalline transformation from basic carbonates to mesoporous metal oxides. The crystal interconversion not only endows the crystallinity and mesoporosity of oxides but also generates abundant surface-step defects that show remarkable enhancement of the catalytic activity of porous oxides. Our method likely provides an alternative paradigm for cost-effective and universal synthesis of crystalline mesoporous oxides beyond the traditional templating methods.

INTRODUCTION

There has been a substantial amount of interest in nanostructured mesoporous oxides with large accessible surface areas/pore volumes.[1–12] Given fast transport and dispersion of electrons/reactants, nanostructured porous oxides show promising applications in a number of fields, e.g., catalysis,[13,14] energy storage,[15–19] and nanomedicines.[20,21] Amorphous oxides even with mesoporosity are unlikely to meet the demand in materials with superior properties and functionality. For example, control of the crystallinity and crystalline phases is often of crucial importance for semiconducting oxides as photocatalysts.[22] Synthesis of porous oxides with crystalline walls, however, remains a major challenge in this field. Crystallization of oxides usually occurs along with the growth of crystalline grains that brings large volume shrinkage; therefore, collapse of pores occurs before the crystallization, resulting in the loss of accessible surfaces/pores.[23] In another regard, surface defects, mostly on crystalline materials as structural imperfections and deviations from ideal structures,[24] are intimately associated with specific physicochemical properties, e.g., adsorption.[25] Given their electron/coordination unsaturation,[26–29] surface defects are catalytically more active compared with defect-free surfaces. In the context of mesoporous oxides, surface structural defects are less controllable in amorphous or polycrystalline forms.

Syntheses of mesoporous oxides rely on the use of templates. Porosity is typically generated by sacrificial templates that fill the pores during synthesis and are removed afterward.[30–32] A typical example is the use of soft templates such as organic surfactants or block copolymers that co-assemble with metal ions in a solgel process and then are removed to expose the pores. To crystallize mesoporous oxides during templated synthesis, the common solution is to use hard templates or convert soft templates to thermally stable carbon[33,34] or silica[35] at elevated temperatures. Despite great progress that has made in templating methods, the use of sacrificial templates, regardless of soft or hard templates, is costly and time consuming. Since the sol-gel transition is utilized to convert inorganic precursors (e.g., metal salt) to crystalline oxides through calcination, there is a significant kinetic barrier limiting the crystallinity of oxides in solid states. As a consequence, traditional templating methods do not provide an effective solution toward the preparation of nanostructured mesoporous oxides with crystalline walls.[36,37]

Progress and Potential

There has been a tremendous upsurge of interest in crystalline mesoporous transition metal oxides that have enormous potential for applications such as catalysis, energy conversion and storage, separation, and biomedicines. Traditional syntheses of mesoporous oxides rely on the use of templates, which ultimately bring a great challenge in the balance of crystallinity and porosity at the mesoscale. Improving crystallinity of oxides usually occurs along with the growth of crystalline grains, leading to the collapse of mesostructures. Here, we demonstrate the template-free method to meet these challenges. By low-temperature crystal interconversion, the prepared crystalline mesoporous oxides are shown to have abundant surfacestep defects that strongly correlate with the activity of oxides. This synthetic approach is applicable to a number of transition metal oxides, providing a powerful tool to engineer their crystallinity and porosity as well as their catalytic activity.

Here, we report a template-free strategy to synthesize high-quality mesoporous and crystalline transition metal oxides. To avoid the thermal crystallization of oxides from its amorphous sol, our synthetic concept is to use conversion of highly crystalline basic carbonate salts (i.e., $M(OH)_2CO_3$) to metal oxides (Figure 1A).[38,39] Simultaneously, the removal of small molecules such as CO_2 and H_2O creates mesoscopic porosity in the size range of 3–8 nm within metal oxides in the absence of any templates. Since most basic carbonate salts have a low thermal

decomposition temperature, the elimination of non-metal components effectively avoids the overgrowth of crystal grains and the collapse of pores while maintaining the high crystallinity of oxides. Six mesoporous oxides including Co_3O_4, CoO, $Cu_{0.92}Co_{2.08}O_4$, $MnCo_2O_{4.5}$, $ZnCo_2O_4$, and CuO were synthesized in two-dimensional (2D) nanostructures as nanoplates and nanosheets. Compared with other templating syntheses, our method is unique in that there are abundant surface-step defects as identified on the surface of mesoporous Co_3O_4 nanoplates. Those defect-rich Co_3O_4 nanoplates are proven to have superior catalase- and peroxidase-like activity, about 130-fold more active than the commercial one and 10-fold more active than the mesoporous Co_3O_4 prepared from hard templating. Density functional theory (DFT) calculations further reveal the key role of the surface cobalt step in promoting the activity of Co_3O_4. Our method is therefore expected to provide a new way of preparing nanostructured mesoporous oxides with crystalline walls and defect-rich surfaces that are potentially useful in heterogeneous catalysis.

RESULTS

Synthesis of $Co_2(OH)_2CO_3$ and Co_3O_4 Nanoplates

The synthetic methodofoxide nanoplatesisschematically presented inFigure1A. Using mesoporous Co_3O_4 as an example, nanoplates of cobalt hydroxide carbonate ($Co_2(OH)_2CO_3$) were synthesized through a hydrothermal method. Cobalt(II) nitrate ($Co(NO_3)_2$) was first mixed with urea in water/ethanol in the presence of oleic acid as stabilizers. The mixture was heated to 160C for 9 h in an autoclave. Under this temperature, urea gradually decomposed to form isocyanic acid and ammonia that controlled the pH ofthe solution(Equation 1).Meanwhile, isocyanic acidhydrolyzedinwater further produced CO_2 (Equation 2).[40] As such, $Co(NO_3)_2$ reacted with CO_2 under slightly basic condition to form $Co_2(OH)_2CO_3$ nanoplates capped by oleic acid (Equation 3). As-obtained $Co_2(OH)_2CO_3$ nanoplates were calcined at 300C for 3 h to produce mesoporous Co_3O_4 nanoplates (Equation 4). The corresponding reactions are as follows:

$$NH_2\text{-}CO\text{-}NH_2 / HNCO + NH_3 \quad \text{(Equation 1)}$$

[1]Jiangsu Key Laboratory of New Power Batteries, Collaborative Innovation Center of Biomedical Functional Materials, School of Chemistry and Materials Science, Nanjing Normal University, Nanjing 210023, China

[2]Department of Chemistry, University of Connecticut, Storrs, CT 06269, USA

[3]Institute of Materials Science, University of Connecticut, Storrs, CT 06269, USA

[4]Green Emulsions, Micelles, and Surfactants Center, University of Connecticut, Storrs, CT 06269, USA

[5]International Collaborative Laboratory of 2D Materials for Optoelectronics Science and Technology of Ministry of Education, Institute of Microscale Optoelectronics, Shenzhen University, Shenzhen 518060, China

[6]These authors contributed equally

[7]Lead Contact

*Correspondence: ben.liu@njnu.edu.cn (B.L.), yuanyuan.2.zhu@uconn.edu (Y.Z.), steven.suib@uconn.edu (S.L.S.), jie.he@uconn.edu (J.H.) https://doi.org/10.1016/j.matt.2020.02.002

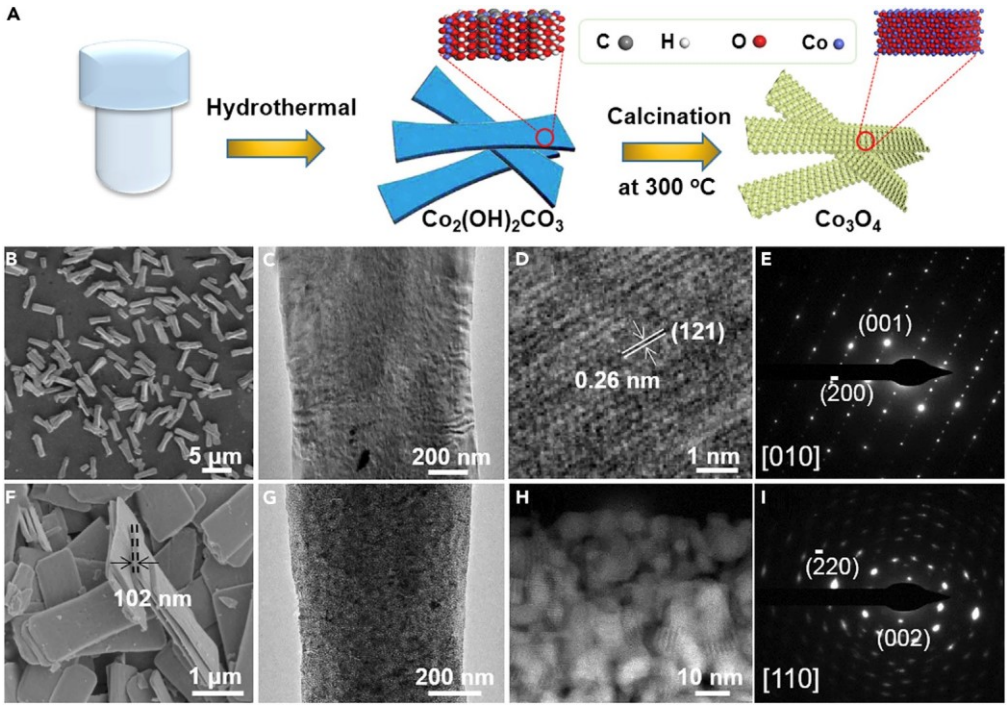

Figure 1. Synthesis and Microscopic Characterization of $Co_2(OH)_2CO_3$ and Co_3O_4 Nanoplates (A) Synthetic scheme of mesoporous Co_3O_4 nanoplates.

(B and C) SEM (B) and TEM (C) images of $Co_2(OH)_2CO_3$ nanoplates.

(D) HRTEM of $Co_2(OH)_2CO_3$.

(E) SAED pattern of $Co_2(OH)_2CO_3$ along the z direction.

(F and G) SEM (F) and TEM (G) images of mesoporous Co_3O_4 nanoplates.

(H) HAADF-STEM image of Co_3O_4 nanoplates.

(I) SAED pattern of mesoporous Co_3O_4.

$$HNCO + H_2O / CO_2 + NH_3 \quad \text{(Equation 2)}$$

$$CO_2 + 4OH + 2Co^{2+} / Co_2(OH)_2CO_3 + H_2O \quad \text{(Equation 3)}$$

$$3Co_2(OH)_2CO_3 + O_2 / 3CO_2 + 3H_2O + 2Co_3O_4 \quad \text{(Equation 4)}$$

Figure 1 shows electron microscopy characterizations of $Co_2(OH)_2CO_3$ and Co_3O_4 nanoplates. Low-magnification scanning electron microscopy (SEM) images confirm monodispersity of the two types of nanoplates with dog-bone-like nanostructures. $Co_2(OH)_2CO_3$ nanoplates have a length of 3.96 G 0.46 mm with a thickness of 130 G 30 nm (Figures S1 and S2). The center width of $Co_2(OH)_2CO_3$ is 0.85 G 0.15 mm while that of the two ends is 1.05 G 0.17 mm. $Co_2(OH)_2CO_3$ nanoplates are densely packed without any obvious porosity under transmission electron microscopy (TEM, Figure 1C). The high-resolution TEM (HRTEM) image in Figure 1D shows clear lattice fringes of $Co_2(OH)_2CO_3$ of about 0.26 nm, assigned to its (121) plane. Figure 1E displays the selected area electron diffraction (SAED) pattern in which

(001) and $(\bar{2}00)$ planes are well resolved along the [010] direction. This is in good agreement with the P21/a space group of monoclinic $Co_2(OH)_2CO_3$. Since the SAED is taken perpendicular to the nanoplate, the growth direction of the $Co_2(OH)_2CO_3$ nanoplate is along [001] while the lateral direction is oriented along [100]. The ordered SAED pattern also reveals single-crystal-like crystallinity of $Co_2(OH)_2CO_3$ nanoplates. After calcination, the nanostructures of 2D plates were

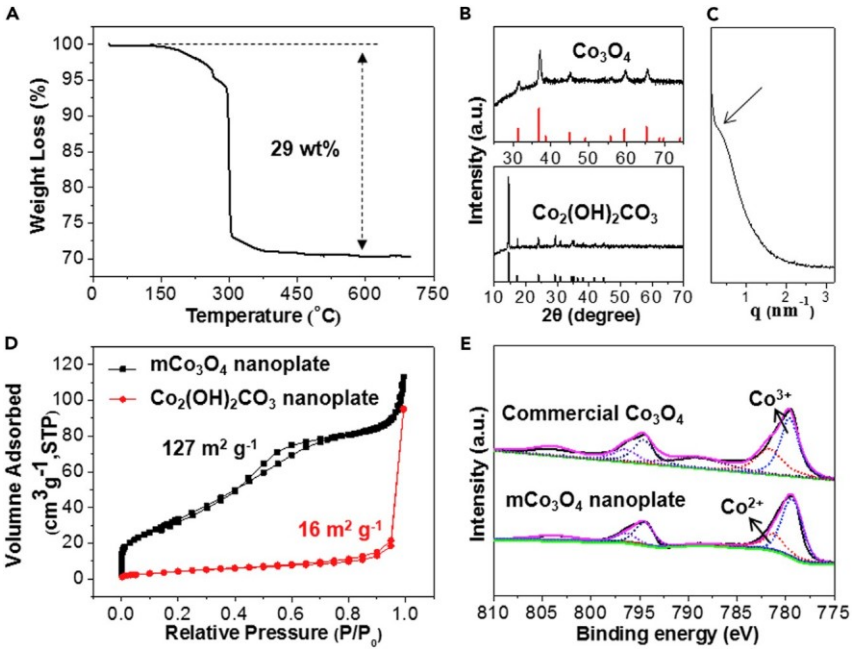

Figure 2. Characterization of Mesoscale Porosity and Crystallinity of Co_3O_4 Nanoplates (A) Thermogravimetric analysis of $Co_2(OH)_2CO_3$ nanoplates.

(B) XRD of $Co_2(OH)_2CO_3$ and Co_3O_4 nanoplates.

(C) SAXS of mesoporous Co_3O_4 nanoplates.

(D) Nitrogen adsorption-desorption isotherm of the mesoporous Co_3O_4 nanoplates and $Co_2(OH)_2CO_3$ solid nanoplates.

(E) Co 2p XPS spectra of the obtained 2D mesoporous Co_3O_4 nanoplates and commercial Co_3O_4.

largely retained while forming the mesoscale porosity in Co_3O_4. The removal of large anions, i.e., OH and CO_3^2, brought about a minor volume shrinkage. The average length and thickness of these mesoporous Co_3O_4 nanoplates are measured as 3.88 G 0.24 mm and 90 G 20 nm (Figure S3), respectively, slightly smaller than those of $Co_2(OH)_2CO_3$ nanoplates. Under dark-field scanning TEM (STEM) (Figure 1H), Co_3O_4 nanoplates showed interconnected small frameworks separated with finite pores throughout in the range of 3–8 nm. The ordered SAED patterns along [110] zone axes confirm the high crystallinity of spinel Co_3O_4 with the space group of Fd3m.

Thermogravimetric analysis (TGA) confirms the thermal decomposition of $Co_2(OH)_2CO_3$ (Figure 2A). The decomposition occurs sharply at 300C with a weight loss of about 29%, consistent with the theoretical weight loss (24 wt %) for the crystalline transition from $Co_2(OH)_2CO_3$ to Co_3O_4. The additional weight loss of 5 wt % is possibly due to the removal of oleic acid that are thermally decomposed around 250C.[41] This was also confirmed by infrared spectroscopy (Figure S4). The crystalline transition from $Co_2(OH)_2CO_3$ to Co_3O_4 was examined by X-ray diffraction (XRD). In line with the TGA analysis, $Co_2(OH)_2CO_3$ (PDF no. 01-079-7085) is readily transformed to spinel Co_3O_4 (PDF no. 090418) as displayed in Figure 2B. The appearance of the small-angle X-ray scattering (SAXS) peak at q value of about 0.55 nm^1 in Figure 2C is indicative of the mesoscale periodicity in Co_3O_4.[42,43] Figure 2D shows the nitrogen sorption isotherms of as-made Co_3O_4 nanoplates. A representative type-IV isotherm of Co_3O_4 nanoplates is characteristic of mesoporosity. The Brunauer-Emmett-Teller (BET) specific surface area is 127 $m^2 g^1$ with an average pore diameter of 4.4 nm calculated by the Barrett-Joyner-Halenda method (Figure S5A). The BET specific surface area of mesoporous Co_3O_4 nanoplates is also comparable with other mesoporous Co_3O_4 materials prepared using soft or

hard templating methods, as summarized in Table S1. In comparison, the BET specific surface area of $Co_2(OH)_2CO_3$ nanoplates is only 16 $m^2 g^1$ without an obviously fine pore distribution (Figures 2D and S5B).

The surface oxidation state of Co was examined using X-ray photoelectron spectroscopy (XPS) (Figures 2E and S6). The Co 2p peaks centered at 779.3 and 794.6 eV are assigned to Co $2p_{3/2}$ and Co $2p_{1/2}$, respectively.[44] The splitting of Co $2p_{3/2}$ and Co $2p_{1/2}$ is 15.3 eV, as typically for Co_3O_4.[45,46] The ratio of Co^{3+}/Co^{2+} is estimated to be 3.2:1 (Figure 2E), which is higher than the theoretical value of Co^{3+}/Co^{2+}.[47] By comparison, the Co^{3+}/Co^{2+} ratio of commercial Co_3O_4 powder is measured as 1.6:1. In addition, the Co^{2+} satellite features became less pronounced in Co_3O_4 nanoplates. The surface composition has been confirmed using secondary ion mass spectrometry (SIMS). As shown in Table S2, the surface Co-to-O ratio of Co_3O_4 nanoplates is approximately 1:5.6 at a sputtering depth of 0.5 nm, while the surface Co-to-O ratio of commercial Co_3O_4 is 1:2.6. These results reveal that mesoporous Co_3O_4 nanoplates have a Co-defect-rich surface (see discussion below).

Synthesis of hydroxide carbonates is a delicate balance of the solution pH and CO_2 concentration.[48] First of all, the solution pH controls the delivery of hydroxide anions. When adding sodium hydroxide directly, the formation of cobalt hydroxides was seen (Figure S7). At the same time, the balanced delivery rate of carbonates anions is extremely important. Again, the direct use of sodium carbonate directly resulted in the formation of cobalt carbonate (Figure S8). In our synthesis, the thermal decomposition of urea was chosen to generate carbonate-containing alkaline solution medium under hydrothermal conditions. Additionally, oleic acid plays a key role in determining the nanoplate structures of $Co_2(OH)_2CO_3$ and balancing the hydrolysis rate of Co^{2+} ions as demonstrated in our control experiments (Figures S9– S11). In the absence of oleic acid, pure Co_3O_4 nanoparticles were formed, while $Co_2(OH)_2CO_3$ was obtained in the presence of oleic acid regardless of solvents, e.g., water, ethanol, or water-ethanol mixtures. Oleate as a strong chelation ligand can bind to Co^{2+} ions and moderate their reactivity. In the absence of oleic acid, Co^{2+} favored the formation of $Co(OH)_2$ thermodynamically with a low-solubility product constant ($K_{sp,\ Co(OH)2}$ = 5.92 3 10^{15}).[49] The $Co(OH)_2$ intermediates further decomposed to Co_3O_4 nanoparticles under high temperatures.[50] Furthermore, oleic acid is critical to control the size of $Co_2(OH)_2CO_3$ nanoplates (Figures S12 and S13). When the concentration of oleic acid varied from 0.17 M to 0.46 M, the average length of $Co_2(OH)_2CO_3$ nanoplates decreased from 4.12 G 0.41 mm to 3.22 G 0.28 mm. The center width of $Co_2(OH)_2CO_3$ nanoplates also decreased slightly from 0.88 G 0.08 mm to 0.83 G 0.12 mm. In addition, the thickness of $Co_2(OH)_2CO_3$ nanoplates also decreased from approximately 150 nm to 90 nm with an increase of oleic acid concentration from 0.17 M to 0.46 M, as displayed in Figure S14.

The formation of mesoporosity relies only on the thermal decomposition of hydroxide carbonates where the removal of small molecules (e.g., CO_2 and H_2O) can template the formation of mesoporosity. As confirmed by TEM in Figures S15 and S16, when annealed at 150C (below thermal decomposition temperature) for 2 h, $Co_2(OH)_2CO_3$ nanoplates remained stable without phase transformation to Co_3O_4. No mesopores were observed. When the thermal annealing temperature increased to 550C, Swiss-cheese-like Co_3O_4 nanoplates with much larger pores

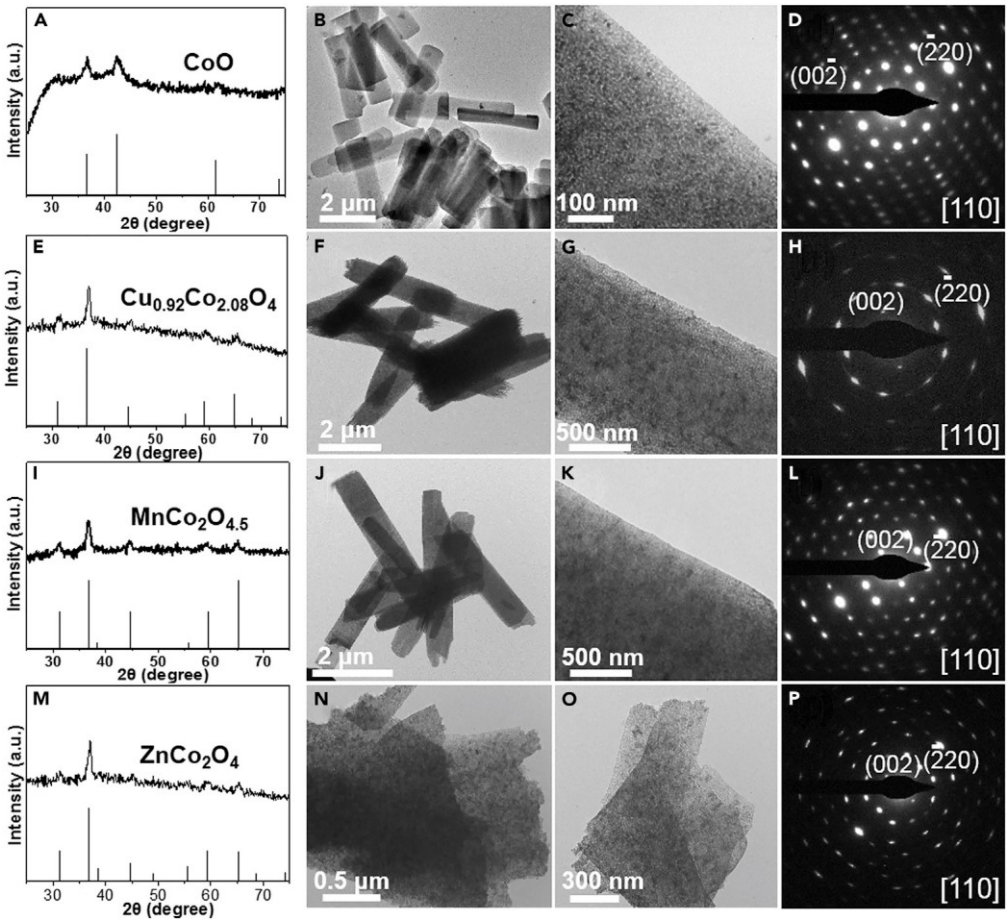

Figure 3. Template-free Syntheses of Other Oxides

(A–D) XRD (A), TEM images (B and C), and SAED (D) of mesoporous CoO nanoplates.

(E–H) XRD (E), TEM images (F and G), and (H) SAED of mesoporous $Cu_{0.92}Co_{2.08}O_4$ nanoplates.

(I–L) XRD (I), TEM images (J and K), and SAED (L) of mesoporous $MnCo_2O_{4.5}$ nanoplates.

(M–P) XRD (M), TEM images (N and O), and SAED (P) of mesoporous $ZnCo_2O_4$ nanosheets.

(43 G 14 nm) were formed. These results suggest that mesoporous Co_3O_4 nanoplates remain thermally unstable and that the pores will collapse at a higher calcination temperature (e.g., 550C). The collapse of mesoporous structures is a result of the growth of Co_3O_4 crystalline domains, as reported previously.[51]

Our synthetic strategy is general and applicable to the preparation of other mesoporous transition metal oxides. First of all, the oxidation state of transition metals is controllable through the calcination atmosphere. Taking $Co_2(OH)_2CO_3$ as an example, calcining $Co_2(OH)_2CO_3$ nanoplates under nitrogen results in the formation of CoO (Figures 3A and S17). In the absence ofoxygen, the oxidation state of Co remains as+2 as presented in $Co_2(OH)_2CO_3$. Second, other transition metals, e.g., Cu, Zn, and Mn with atomic size similar to that of Co, can be doped in $Co_2(OH)_2CO_3$. This further leads to the formation of doped spinel structures after calcination. As examples, three mixed spinel oxides in the form of MCo_2O_4 were prepared (Figures 3 and S18–S21). Among them, $ZnCo_2O_4$ formed 2D nanosheets while the other two showed similar 2D plate-like structures. Lastly, our method has been validated for

other hydroxide carbonates, e.g., $Cu_2(OH)_2CO_3$. Similarly, $Cu_2(OH)_2CO_3$ as precursors can be converted to crystalline mesoporous CuO nanosheets, as displayed in Figure S22.

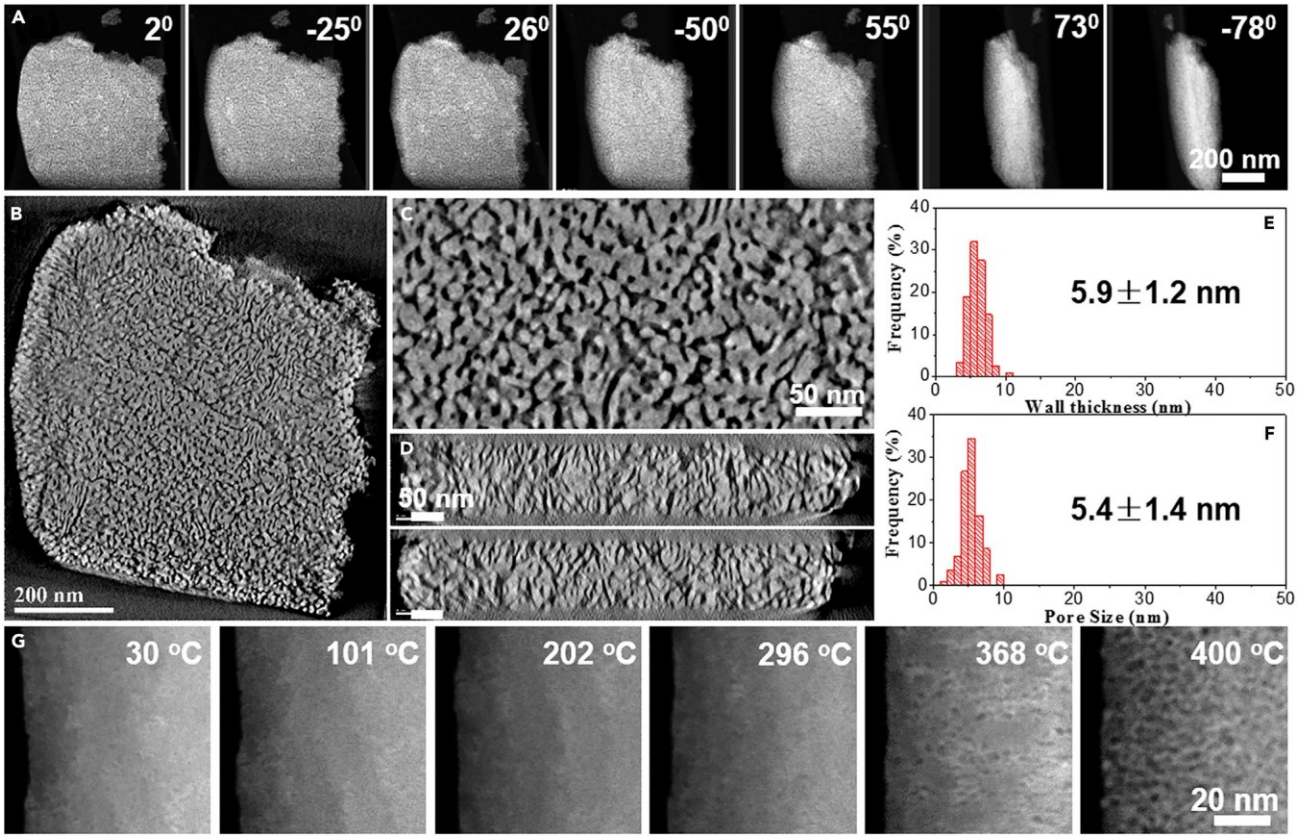

Figure 4. Tomography and In Situ Electron Microscopy Annealing of Mesoporous Co_3O_4 Nanoplates (A–C) Tomography STEM images of crushed Co_3O_4 nanoplates from different observation angles.

(D–F) Reconstructed cross-section image (D), wall thickness of mesopores (E), and pore size distribution (F) of Co_3O_4 nanoplates.

(G) In situ TEM characterizations of $Co_2(OH)_2CO_3$ nanoplates through thermal treatment from room temperature to 400C under vacuum at a heating rate of 10C s^1.

Porosity and Crystallinity of Co_3O_4 Nanoplates

All porous oxides show irregular and disordered mesopores. To investigate the detailed pore structures and distribution, we further used STEM to characterize Co_3O_4 nanoplates. The images were acquired by rotating the samples from 2 to 78 and reconstructed into a 3D tomogram (Video S1). Representative STEM images at tilt angles from 2 to 78 are presented in Figure 4A. The interconnected mesopores were observed throughout Co_3O_4 nanoplates. Figures 4B–4D show the 3D reconstructed surface and cross-section images. It is interesting to point out that Co_3O_4 frameworks and mesopores are bicontinuous, although the porous structures are disordered. The wall thickness is measured as 5.9 G 1.2 nm (Figure 4E) while the pore diameter is approximately 5.4 G 1.4 nm (Figure 4F), slightly larger than that measured from BET. The volume ratio for void is measured as 47.6% G 10%, consistent with the void ratio from BET measurement (approximately 48.3% using the density of Co_3O_4, see Supplemental Information for details). From the reconstructed cross-section images, mesopores are interconnected through vertical channels along the z direction (Video S2). This is likely attributed to the formation mechanism of mesopores. In the process of thermal decomposition of $Co_2(OH)_2CO_3$, the outflow of small molecules such as CO_2 and H_2O templated the formation of mesoscale porosity while simultaneously converting $Co_2(OH)_2CO_3$

to Co_3O_4. The diffusion of those small molecules through vertical channels likely minimizes the diffusion length to the surface of nanoplates.

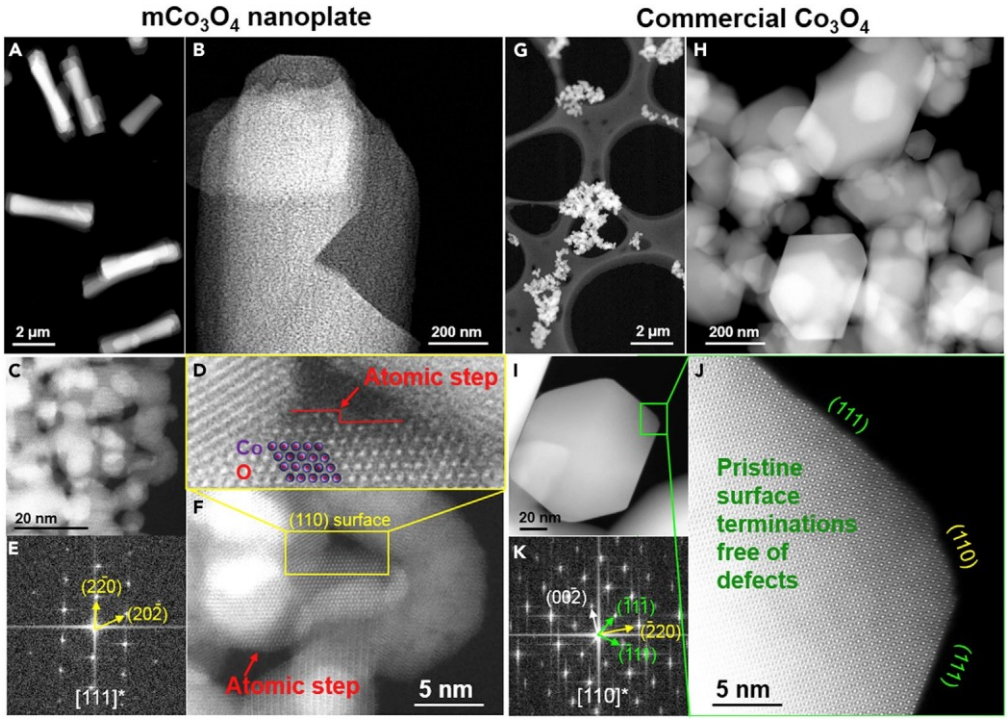

Figure 5. Surface Structure Comparison between Mesoporous Co_3O_4 Nanoplate (mCo_3O_4 Nanoplate) and Commercial Co_3O_4 (A–C) HAADF-STEM observations of mCo_3O_4 nanoplate under different magnifications.

(D) Close-up of the (110) surface termination of mCo_3O_4 nanoplate obtained by enlarging HAADF-STEM image of (F).

(E) Fast Fourier transform (FFT) patterns of (F).

(F) Representative high-resolution HAADF-STEM image of mCo_3O_4 nanoplate in [111] zone axis. The red arrows in (D) and (F) denote atomic steps at the top and bottom (110) surfaces of the mCo_3O_4 nanoplate.

(G–I) HAADF-STEM overviews of commercial Co_3O_4 under different magnifications.

(J) Close-up of the (111) and (110) surface terminations of commercial Co_3O_4 in (I).

(K) Corresponding FFT patterns of (J).

The evolution of mesopores upon heating was monitored through in situ heating STEM (Figure 4G). Since the in situ heating was carried out at a heating rate of 10C per second under vacuum, the temperature does not reflect the thermal decomposition point of $Co_2(OH)_2CO_3$. At 368C, non-uniform pores appeared on the surface. The pore development was seen under higher temperatures (Video S3). After 400C, $Co_2(OH)_2CO_3$ non-porous nanoplates readily transformed to mesoporous Co_3O_4 nanoplates. The in situ experiments align well with the pore-formation mechanism discussed previously.

Representative aberration-corrected high-angle annular dark-field scanning TEM (HAADF-STEM) images of mesoporous Co_3O_4 nanoplates and control commercial Co_3O_4 powders are presented in Figure 5. Low-magnification STEM overviews (Figures 5A–5C and 5G–5I) show densely packed small, bright Co_3O_4 nanoparticles (average size 5.2 G 1.1 nm) and dark pores of the mesoporous Co_3O_4, in contrast to the large Co_3O_4 particles (100–300 nm) of the commercial Co_3O_4. This direct visual comparison highlights the advantage of mesoporous structures in providing a high specific surface area, as also confirmed by the above nitrogen adsorption-desorption measurement. High-resolution HAADF-STEM of mesoporous Co_3O_4

nanoplates suggests a high degree ofcrystallinity (Figures 5D, 5F, S23, and S24), agreeing wellwith our SAED shown in Figure 1. Importantly, the excellent crystallinity leads to faceted Co_3O_4 nanoparticles with both high- and low-index terminations.

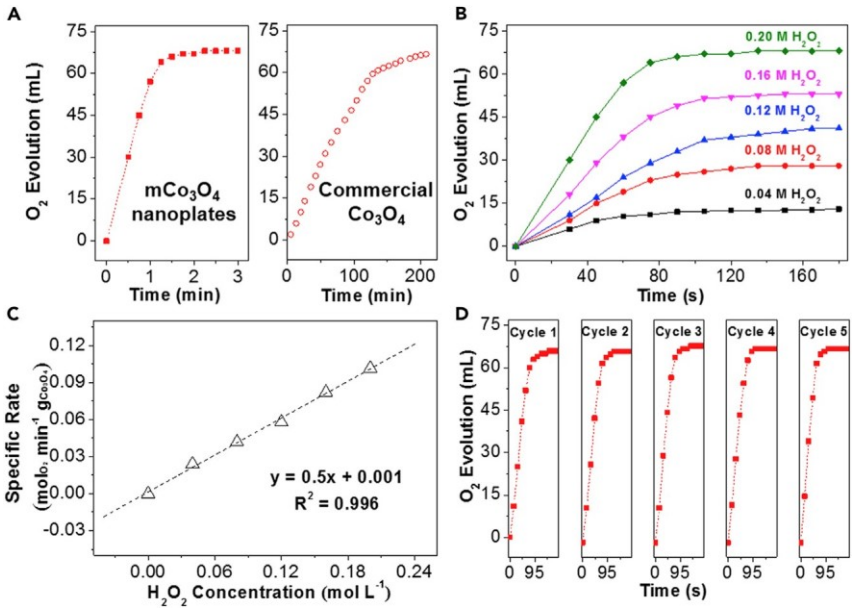

Figure 6. Catalase-like Activity of Mesoporous Co_3O_4 Nanoplates

(A) Oxygen evolution volume as a function of time over mesoporous Co_3O_4 nanoplate and commercial Co_3O_4 catalysts.

(B) Oxygen evolution volume as a function of time over the mesoporous Co_3O_4 nanoplate at varied H_2O_2 concentrations.

(C) The plots of specific O_2 evolution rate against H_2O_2 concentrations.

(D) Recycling stability test over the mesoporous Co_3O_4 nanoplate.

Of some of the low-index surface terminations, for example the top and bottom (110) terminations in Figures 5D–5F and S24, surface steps of one atomic layer in height with missing Co columns were observed. Unlike the pristine surface terminations observed in the commercial Co_3O_4 catalyst (Figures 5J and S25), the presence of these surface steps and high-index terminations (Figure S24B) at the surface of the mesoporous Co_3O_4 exposes more undercoordinated surface sites. The missing surface Co observed by aberration-corrected HAADF-STEM agrees well with the above XPS and SIMS characterizations, where an average Co valence increases and the surface Co-to-O ratio decreases as derived from the surface Co step defects. These undercoordinated surface Co steps are potentially catalytically active. As a comparison, no obvious surface steps or other defects were observed at the dominant (111) terminations of commercial Co_3O_4 nanoparticles. Considering the extraordinarily high surface areas of the mesoporous structure, a large number of such imperfect surface terminations can be expected and could be responsible for the observed high catalytic activity.

Catalytic Activity and DFT Simulation

Co_3O_4 shows catalase-like activity that catalyzes the decomposition of peroxides to O_2 as reported previously.[52,53] Using H_2O_2 decomposition, we further evaluated catalase-like activity of mesoporous Co_3O_4 nanoplates. To measure the catalaselike activity, we mixed mesoporous Co_3O_4 nanoplates with H_2O_2 and monitored the production rate/volume of O_2 as a function of reaction time. In less than 1 min, 95% of H_2O_2 conversion was seen when using mesoporous Co_3O_4 nanoplates as catalysts (Figure 6A). Over commercial Co_3O_4, it took more than 100 min

to reach a similar conversion. The initial production rate of O_2 estimated from the first-order kinetic fitting is 0.13 mol$min^{1} per 1 g of catalyst for mesoporous Co_3O_4 nanoplates. This is roughly 130-fold more active compared with commercial Co_3O_4 (1.1 mmolmin^{1}g^{1}).

Figure 6B shows the kinetic curves of O_2 production at different concentrations of H_2O_2. The production of O_2 increased stoichiometrically with the concentration of H_2O_2, indicating the full conversion of H_2O_2 for all experiments. In the concentration range of H_2O_2 from 0.04 to 0.2 M, there is a linear correlation between the O_2 formation rate and the H_2O_2 concentration. This is indicative of high and stable reactivity of mesoporous Co_3O_4 nanoplates that is not a kinetic barrier for the reaction. The excellent catalytic stability of Co_3O_4 nanoplates is further demonstrated in the recycling experiments. As demonstrated in Figure 6D, after five catalytic cycles mesoporous Co_3O_4 nanoplates retained superior activity without any activity loss.

As controls, we prepared mesoporous Co_3O_4 using hard templating, which has a high BET specific surface area of 117 m^2 g^{1} (Figure S26).[54] The production rate of O_2 normalized to the BET surface area was compared using the two mesoporous Co_3O_4. The formation rate of O_2 is 0.11 mmolmin^{1}m^2 for mesoporous Co_3O_4 prepared from hard templating, while it is 1.03 mmolmin^{1}m^2 for mesoporous Co_3O_4 nanoplates, about 9.4-fold more active than mesoporous Co_3O_4 using a traditional hard templating method. The activity of mesoporous Co_3O_4 nanoplates has been compared with previous literature, as summarized in Table S3. The turnover frequency of our mesoporous Co_3O_4 nanoplates for catalase-like activity is 31.3 min^{1}, much higher than reported values (0.3–5 min^{1}). We therefore consider that the surface-step defects contributed largely toward enhancing the catalase-like activity of Co_3O_4. Furthermore, we demonstrated the application of Co_3O_4 nanoplates as peroxidase-like nanozymes. The oxidation kinetics of 3,3^{0},5,5^{0}-tetramethylbenzidine (TMB) shows that mesoporous Co_3O_4 nanoplates are 3-fold more active compared with mesoporous Co_3O_4 prepared from hard templating (Figure S27).

To understand the underlying mechanism of surface-step defects in promoting catalase-like activity, we carried out DFT calculations on Co_3O_4(110) facet with and without surface Co steps. The (110) facet has a low surface free energy of 0.24 eV/A$^{\circ}$ ^{2}, and the Wulff construction has suggested the presence of surface Co step defects on (110) (Figures S28 and S29). The overall reaction pathways of H_2O_2, including H_2O_2 adsorption, O–O bond scission, H transfer to OH, O*+O* recombination, and O_2 molecule formation, over ideal and defective Co_3O_4(110) are listed in Figures 7A, 7B, and S30. Along these reaction pathways, the formation of two O* species toward the O* collision reaction is generically unfavorable. The surface free energy barrier of the formation of two O* species over ideal Co_3O_4(110) is 4.41 eV, while it is significantly higher than that over defective Co_3O_4(110), 0.15 eV. The reaction snapshots suggest that the step defects are responsible for the adsorption of two O* species. One of the O* species is stabilized by two Co atoms on the step edges that are likely accountable for the low thermodynamic barrier. Similarly, the O*+O* recombination to O_2 occurs on the defective edge. The simulation results suggest that the step-defect edge is catalytically more active than the non-defective surface.

According to previous reports, the scission of O–O bond of H_2O_2 is the rate-determining step of H_2O_2 decomposition.[55,56] We further used the nudged elastic band (NEB) method to investigate the activation energy barrier of O–O bond scission on ideal and defective Co_3O_4(110). Surprisingly, the O–O bond scission is barrier-free over the defective Co_3O_4(110) and the adsorbed H_2O_2* is readily cleaved to OH*

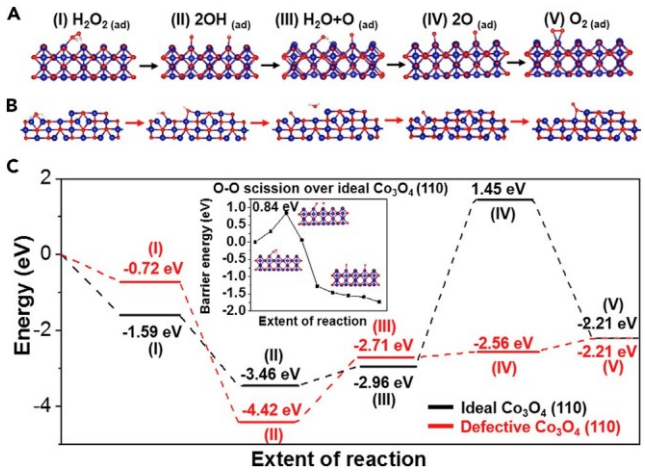

Figure 7. Reaction Energy Diagram of H_2O_2 Decomposition over Defective and Ideal Co_3O_4

(A and B) Reaction steps simulated by DFT for H_2O_2 decomposition over ideal Co_3O_4(110) (A) and defective Co_3O_4(110) (B).

(C) Reaction energy diagram of ideal Co_3O_4(110) and defective Co_3O_4(110). The inset is O–O scission barriers and corresponding configurations over the ideal Co_3O_4(110).

(Figure S31). By comparison, the O–O bond scission has a much higher energy barrier over the ideal Co_3O_4(110) as displayed in the inset of Figure 7C. There is a 0.84 eV energy uphill for the transformation from H_2O_2* to OH* over ideal Co_3O_4(110), leading to a low reactivity of ideal Co_3O_4(110). The great activation-barrier difference of O–O bond scission of ideal Co_3O_4(110) is correlated with the surface Co coordination. As revealed in Figure S28, defective Co_3O_4(110) surface has abundant dangling Co sites that are not present in the ideal Co_3O_4(110). Those sites are beneficial in transforming H_2O_2* to more stable OH*.

DISCUSSION

To summarize, a template-free synthetic method was developed to prepare mesoporous transition metal oxides with highly crystalline walls. Unlike traditional templated growth of mesoporous oxide, our synthesis utilizes the elimination and diffusion of small molecules such as CO_2 and H_2O to generate pores/channels in mesoscale. Well-defined nanoplates of highly crystalline basic carbonates were firstly prepared through hydrothermal synthesis and then converted to mesoporous metal oxides through thermal transformation. Upon annealing around 300C, the thermal transformation of basic carbonates to metal oxides occurred while preserving the high crystallinity of basic carbonates and producing mesopores alongside gaseous by-products, i.e., CO_2 and H_2O. The method is versatile and the synthesis of six mesoporous oxides such as CuO, CoO, and spinel MCo_2O_4 (M = Co, Cu, Mn, and Zn) have been demonstrated. Using STEM tomography, mesopores were found to form continuous, vertical channels within 2D nanostructures of oxides. Aberration-corrected HAADF-STEM reveals the presence of abundant surface-step defects that are unique features of mesoporous Co_3O_4 prepared by our thermal transformation method. Defect-rich mesoporous Co_3O_4 nanoplates exhibit excellent catalase-like activity 10-fold higher than the mesoporous Co_3O_4 prepared using hard templates. Surface Co step defects were found to stabilize O* species and significantly reduce the activation barrier of O–O bond session.

Our synthetic method, as an alternative to traditional templating synthesis, provides an out-of-box solution to prepare crystalline porous oxides. These syntheses of porous oxides are significantly more effective in terms of simplified protocols, materials cost, and volume-time output. Since the sol-gel transition is not involved, the interconversion of two crystals largely

improves the crystallinity of oxides and limits the formation of amorphous oxides. As a general method, the strategy to eliminate small molecules to create bicontinuous pores at the mesoscale is general and is applicable to a library of metastable metal salts not limited to basic carbonates, such as bicarbonates and oxalates. The thermal decomposition of these metal salts ideally will similarly lead to the formation of mesoporous oxides. Additionally, our method also fills the gap of template-free syntheses at the mesoscale. In the past, template-free syntheses of porous materials showed precious little control of pores in microscale or at the molecular level in single-crystalline materials, e.g., zeolites[57] and metal-organic frameworks.[58] Our synthetic strategy is amenable to the current template-free synthesis of porous materials in a broad range of pore sizes, shapes, and nanostructures.

EXPERIMENTAL PROCEDURES

Synthesis of Mesoporous Co_3O_4 Nanoplates

In a typical synthesis of mesoporous Co_3O_4 nanoplates, 0.5154 g of urea was firstly dissolved in 10 mL of deionized water to obtain a homogeneous solution. Thereafter, 15 mL of ethanol was added to the solution and stirred for 30 min. Oleic acid (4 mL) was then added to this solution and stirred for another 30 min to make a homogeneous system. Ten milliliters of 86 mM cobalt(II) nitrate solution was further added to the above system in 30 min. The whole solution was further stirred for 1 h and transferred into a Teflon-lined stainless-steel autoclave. The autoclave was sealed and maintained at 160C for 9 h. When the autoclave was cooled to ambient temperature, the resulting precipitate was isolated by centrifugation and washed several times with hexane, pure water, and ethanol. Finally, the obtained product was dried in vacuum at 40C overnight and calcined in air at 300C for 3 h.

Characterization

The crystallographic structure of the obtained product was analyzed by powder XRD (Bruker D8 Focus X-ray diffractometer, Cu Ka radiation, l = 0.1542 nm). XPS analysis was conducted on an ESCALAB 250 Xi X-ray photoelectron spectrometer with Al Ka radiation. The specific surface area measurement was conducted on a Quantachromeautosorb IQ2 instrument (Quantachrome Instruments). Compact SIMS was utilized to analyze the surface element composition of samples taking a dynamic mode. The ion beam and sputtering time is adjustable to optimize corresponding signals. TEM analysis and in situ heating STEM were carried out on a Talos F200X FEG TEM/STEM operating at 200 kV. Elemental mappings were collected by a Super X system equipped with four Silicon Drift Detectors offering a total collection angle of 0.9 srad. The high-resolution STEM images were collected via a Titan Themis 60300 equipped with a probe corrector to correct condenser lens aberration leading to 0.08 nm spatial resolution at 300 kV. The convergence angle is 25 mrad and HAADFSTEM collection angle 70–200 mrad. Electron tomography image series were acquired in HAADF-STEM mode with 10 mrad convergence angle and 30–200 mrad collection angle. The 3D volumes were reconstructed with IMOD software, visualized, and analyzed with Avizo.

Evaluation of Catalytic Performance

The catalase-like catalytic activity of mesoporous Co_3O_4 nanoplates for H_2O_2 decomposition was evaluated at room temperature. In a typical reaction, 20 mg of catalysts were added to 25 mL of water in a flask and sonicated to obtain a welldispersed suspension. Before injection of H_2O_2, the flask was sealed tightly and purged with N_2 for 20 min to remove air. Subsequently, H_2O_2 with varied concentrations was injected into the flask under stirring. The volume of the produced oxygen was measured every 15 s until the total volume of oxygen became saturated. The reaction rate constant k was calculated based on a reported method.[59] The stability test of the obtained mesoporous Co_3O_4 nanoplates is carried out by recycling the postreaction

mesoporous Co_3O_4 nanoplates (as collected by centrifugation) for five cycles. The measurements with different amounts of H_2O_2 were conducted similarly under otherwise similar conditions.

The peroxidase-like catalytic activity was measured using TMB as a substrate over Co_3O_4. Typically, 0.25 mM TMB, 50 mM H_2O_2, and 10 mg/mL Co_3O_4 catalyst were mixed in sodium acetate buffer (3 mL, pH 5) in a 3.5-mL quartz cell. The reaction kinetics was monitored by the absorbance at 652 nm as a function of time (from 0 min to 10 min).[53]

DFT Calculations

DFT calculations were carried out by using spin-polarized Kohn-Sham DFT. We used the generalized gradient approximation with the Perdew-Burke-Ernzerhof exchange-correlation functional as conducted in the Vienna Ab Initio Simulation Package. The valence orbitals of Co (3d, 4s), O (2s, 2p), C (2s, 2p), and H (1s) were described by plane-wave basis sets with cutoff energies of 400 eV. The Gaussian smearing method with a width of 0.20 eV was used. According to the experimental characterization results, Co_3O_4 with a space group of F-43m was used to model the catalyst structure. Bulk optimization yielded lattice parameters of a = b = c = 8.065 A˚ . The periodic slab model of Co_3O_4(110) was used to simulate the H_2O_2 decomposition reactivity. The Co_3O_4(110) surface was modeled by p(2 3 2) four-atomic-layer supercells with the bottom two layers fixed, and the vacuum gap was set as 15 A˚ to avoid the interaction between the periodic images. Defective Co_3O_4(110) was constructed by deleting half a layer of Co and O atoms. All of the atoms in the structure were relaxed during the calculation. The Brillouin zone was sampled at (2 3 2 3 1). The convergence criteria for the energy and force were set to 10^4 eV and 0.02 eV/A˚ . For evaluating the energy barriers, all transition states and pathways were computed using the climbing image NEB method. The adsorption energies were calculated according to the equation, E_{ads} = E(adsorbate/substrate) [E(substrate) + E(adsorbate)], where E(adsorbate/substrate), E(adsorbate), and E(substrate) are energies of the substrate with the adsorbate, the gas-phase molecule, and the clean substrate, respectively. The reaction energy and barrier were calculated by E_r = E(FS) E(IS) and E_a = E(TS) E(IS), where E(IS), E(FS), and E(TS) are the energies of the corresponding initial state (IS), final state (FS), and transition state (TS), respectively. The NEB method generally employed to investigate saddle points and minimum energy paths between reactants and products was conducted to reveal the energy barrier of O–O bond scission of ideal and defective Co_3O_4(110).

Additional Information

Synthetic procedures of other mesoporous oxide nanoplates/nanosheets, additional electron microscopic images, SAED and XRD patterns, BET measurements, XPS spectra, and DFT details are available free of charge on the website.

DATA AND CODE AVAILABILITY

The data supporting the findings of this study are available for the article and Supplemental Information, or from the corresponding authors upon request.

SUPPLEMENTAL INFORMATION

Supplemental Information can be found online at https://doi.org/10.1016/j.matt.2020.02.002.

ACKNOWLEDGMENTS

J.H. is grateful for financial support from the National Science Foundation (CBET1705566) and the startup fund from the University of Connecticut. S.L.S. acknowledges the support of the National Science Foundation under award 1803343 of the CBET Division. The SEM/TEM studies were performed using the facilities in the UConn/Thermo Fisher Scientific Center for Advanced Microscopy and Materials Analysis (CAMMA). We thank Dr. Lichun Zhang at the CAMMA (UConn) for his help in SAED analysis. We also acknowledge Dr. Zachary Tobin for his kind help with in situ heating STEM characterization.

AUTHOR CONTRIBUTIONS

M.H., B.L., and J.H. conceived the idea and co-wrote the manuscript. M.H. carried out the synthesis of materials. W.Y. conducted the DFT calculations. H.T. did the in situ heating STEM and tomographic characterizations. L.J. carried out other electron microscopy measurements. L.Z. and M.H. carried out the catalytic evaluations.

P.K., Y.D., and S.L.S. performed XPS/SIMS characterizations and analysis. S.L.S. and S.D. did the BET measurements and analysis. Y.Z. and S.S. carried out the aberration-corrected STEM characterizations and Wulff construction. All authors discussed the results and commented on the manuscript.

DECLARATION OF INTERESTS

The authors declare no competing interests.

Received: December 13, 2019
Revised: January 13, 2020
Accepted: February 5, 2020
Published: March 4, 2020

REFERENCES

1. Kresge, C.T., Leonowicz, M.E., Roth, W.J., Vartuli, J.C., and Beck, J.S. (1992). Ordered mesoporous molecular sieves synthesized by a liquid-crystal template mechanism. Nature 359, 710–712.

2. Beck, J.S., Vartuli, J.C., Roth, W.J., Leonowicz, M.E., Kresge, C.T., Schmitt, K.D., Chu, C.T.W., Olson, D.H., Sheppard, E.W., McCullen, S.B., et al. (1992). A new family of mesoporous molecular sieves prepared with liquid crystal templates. J. Am. Chem. Soc. 114, 10834– 10843.

3. Zhao, D., Feng, J., Huo, Q., Melosh, N., Fredrickson, G.H., Chmelka, B.F., and Stucky, G.D. (1998). Triblock copolymer syntheses of mesoporous silica with periodic 50 to 300 angstrom pores. Science 279, 548–552.

4. Yang, P., Zhao, D., Margolese, D.I., Chmelka, B.F., and Stucky, G.D. (1998). Generalized syntheses of large-pore mesoporous metal oxides with semicrystalline frameworks. Nature 396, 152–155.

5. Kleitz, F., Hei Choi, S., and Ryoo, R. (2003). Cubic Ia3d large mesoporous silica: synthesis and replication to platinum nanowires, carbon nanorods and carbon nanotubes. Chem. Commun. 2136–2137, https://doi.org/10.1039/b306504a.

6. Meng, Y., Gu, D., Zhang, F., Shi, Y., Yang, H., Li, Z., Yu, C., Tu, B., and Zhao, D. (2005). Ordered mesoporous polymers and homologous carbon frameworks: amphiphilic surfactant templating and direct transformation. Angew. Chem. Int. Ed. 44, 7053–7059.

7. Yang, H., Coombs, N., and Ozin, G.A. (1997). Morphogenesis of shapes and surface patterns in mesoporous silica. Nature 386, 692–695.

8. Ren, Y., Ma, Z., and Bruce, P.G. (2012). Ordered mesoporous metal oxides: synthesis and applications. Chem. Soc. Rev. 41, 4909–4927.

9. Gu, D., and Schu¨th, F. (2014). Synthesis of nonsiliceous mesoporous oxides. Chem. Soc. Rev. 43, 313–344.

10. Lu, Y., Fan, H., Stump, A., Ward, T.L., Rieker, T., and Brinker, C.J. (1999). Aerosol-assisted selfassembly of mesostructured spherical nanoparticles. Nature 398, 223–226.

11. Weng, W., Higuchi, T., Suzuki, M., Fukuoka, T., Shimomura, T., Ono, M., Radhakrishnan, L., Wang, H., Suzuki, N., Oveisi, H., and Yamauchi, Y. (2010). A high-speed passive-matrix electrochromic display using a mesoporous TiO_2

electrode with vertical porosity. Angew. Chem. Int. Ed. 49, 3956–3959.

12. Yamauchi, Y., Nagaura, T., Ishikawa, A., Chikyow, T., and Inoue, S. (2008). Evolution of standing mesochannels on porous anodic alumina substrates with designed conical holes. J. Am. Chem. Soc. 130, 10165– 10170.

13. Li, H., Bian, Z., Zhu, J., Zhang, D., Li, G., Huo, Y., Li, H., and Lu, Y. (2007). Mesoporous titania spheres with tunable chamber structure and enhanced photocatalytic activity. J. Am. Chem. Soc. 129, 8406–8407.

14. Kuo, C.-H., Mosa, I.M., Poyraz, A.S., Biswas, S., El-Sawy, A.M., Song, W., Luo, Z., Chen, S.-Y., Rusling, J.F., He, J., and Suib, S.L. (2015). Robust mesoporous manganese oxide catalysts for water oxidation. ACS Catal. 5, 1693–1699.

15. Liang, H.-W., Bru¨ller, S., Dong, R., Zhang, J., Feng, X., and Mu¨llen, K. (2015). Molecular metal-N_x centres in porous carbon for electrocatalytic hydrogen evolution. Nat. Commun. 6, 7992.

16. Rosen, J., Hutchings, G.S., and Jiao, F. (2013). Ordered mesoporous cobalt oxide as highly efficient oxygen evolution catalyst. J. Am. Chem. Soc. 135, 4516–4521.

17. Shaju, K.M., Jiao, F., De´bart, A., and Bruce, P.G. (2007). Mesoporous and nanowire Co_3O_4 as negative electrodes for rechargeable lithium batteries. Phys. Chem. Chem. Phys. 9, 1837–1842.

18. Zhong, W., Huang, J., Liang, S., Liu, J., Li, Y., Cai, G., Jiang, Y., and Liu, J. (2019). New Prelithiated V_2O_5 superstructure for lithium-ion batteries with long cycle life and high power. ACS Energy Lett. 5, 31–38.

19. Liu, J., Tang, S., Lu, Y., Cai, G., Liang, S., Wang, W., and Chen, X. (2013). Synthesis of Mo_2N nanolayer coated MoO_2 hollow nanostructures as high-performance anode materials for lithium-ion batteries. Energy Environ. Sci. 6, 2691–2697.

20. Li, Z., Barnes, J.C., Bosoy, A., Stoddart, J.F., and Zink, J.I. (2012). Mesoporous silica nanoparticles in biomedical applications. Chem. Soc. Rev. 41, 2590–2605.

21. Ariga, K., Vinu, A., Yamauchi, Y., Ji, Q., and Hill, J.P. (2012). Nanoarchitectonics for mesoporous mater. Bull. Chem. Soc. Jpn. 85, 1–32.

22. Chen, X., and Mao, S.S. (2007). Titanium dioxide nanomaterials: synthesis, properties, modifications, and applications. Chem. Rev. 107, 2891–2959.

23. Li, D., Zhou, H., and Honma, I. (2004). Design and synthesis of self-ordered mesoporous nanocomposite through controlled in-situ crystallization. Nat. Mater. 3, 65–72.

24. Kofstad, P. (1996). Defect chemistry in metal oxides. Phase Transit. 58, 75–93.

25. Sun, Q., Cortie, D., Zhang, S., Frankcombe, T.J., She, G., Gao, J., Sheppard, L.R., Hu, W., Chen, H., Zhuo, S., et al. (2017). The formation of defect-pairs for highly efficient visible-light catalysts. Adv. Mater. 29, 1605123.

26. Tuller, H., and Nowick, A. (1979). Defect structure and electrical properties of nonstoichiometric CeO_2 single crystals. J. Electrochem. Soc. 126, 209–217.

27. Pacchioni, G. (2008). Modeling doped and defective oxides in catalysis with density functional theory methods: room for improvements. J. Chem. Phys. 128, 182505.

28. Schweke, D., Mordehovitz, Y., Halabi, M., Shelly, L., and Hayun, S. (2018). Defect chemistry of oxides for energy applications. Adv. Mater. 30, 1706300.

29. Zhou, Y., Zhang, Z., Fang, Z., Qiu, M., Ling, L., Long, J., Chen, L., Tong, Y., Su, W., Zhang, Y., et al. (2019). Defect engineering of metal-oxide interface for proximity of photooxidation and photoreduction. Proc. Natl. Acad. Sci. U S A 116, 10232–10237.

30. Malgras, V., Ji, Q., Kamachi, Y., Mori, T., Shieh, F.-K., Wu, K.C.-W., Ariga, K., and Yamauchi, Y. (2015). Templated synthesis for nanoarchitectured porous materials. Bull. Chem. Soc. Jpn. 88, 1171–1200.

31. Dahal, N., Ibarra, I.A., and Humphrey, S.M. (2012). High surface area mesoporous Co_3O_4 from a direct soft template route. J. Mater. Chem. 22, 12675–12681.

32. Jiang, B., Guo, Y., Kim, J., Whitten, A.E., Wood, K., Kani, K., Rowan, A.E., Henzie, J., and Yamauchi, Y. (2018). Mesoporous metallic iridium nanosheets. J. Am. Chem. Soc. 140, 12434–12441.

33. Lee, J., Christopher Orilall, M., Warren, S.C., Kamperman, M., DiSalvo, F.J., and Wiesner, U. (2008). Direct access to thermally stable and highly crystalline mesoporous transition-metal oxides with uniform pores. Nat. Mater. 7, 222–228.

34. Zhang, R., Tu, B., and Zhao, D. (2010). Synthesis of highly stable and crystalline mesoporous anatase by using a simple surfactant sulfuric acid carbonization method. Chem. Eur. J. 16, 9977–9981.

35. Liu, B., Luo, Z., Federico, A., Song, W., Suib, S.L., and He, J. (2015). Colloidal amphiphiletemplated growth of highly crystalline mesoporous nonsiliceous oxides. Chem. Mater. 27, 6173–6176.

36. Oveisi, H., Rahighi, S., Jiang, X., Nemoto, Y., Beitollahi, A., Wakatsuki, S., and Yamauchi, Y. (2010). Unusual antibacterial property of mesoporous titania films: drastic improvement by controlling surface area and crystallinity. Chem. Asian J. 5, 1978–1983.

37. Zhang, L., Jin, L., Liu, B., and He, J. (2019). Templated growth of crystalline mesoporous materials: from soft/hard templates to colloidal templates. Front. Chem. 7, 22.

38. Xiong, S., Chen, J.S., Lou, X.W., and Zeng, H.C. (2012). Mesoporous Co_3O_4 and CoO@C topotactically transformed from chrysanthemum-like $Co(CO_3)_{0.5}(OH)$$0.11H_2O$ and their lithium-storage properties. Adv. Funct. Mater. 22, 861–871.

39. Hu, L., Peng, Q., and Li, Y. (2008). Selective synthesis of Co_3O_4 nanocrystal with different shape and crystal plane effect on catalytic property for methane combustion. J. Am. Chem. Soc. 130, 16136–16137.

40. Yim, S.D., Kim, S.J., Baik, J.H., Nam, I.S., Mok, Y.S., Lee, J.-H., Cho, B.K., and Oh, S.H. (2004). Decomposition of urea into NH_3 for the SCR process. Ind. Eng. Chem. Res. 43, 4856–4863.

41. Wilson, D., and Langell, M.A. (2014). XPS analysis of oleylamine/oleic acid capped Fe_3O_4 nanoparticles as a function of temperature. Appl. Surf. Sci. 303, 6–13.

42. Liu, B., Kuo, C.-H., Chen, J., Luo, Z., Thanneeru, S., Li, W., Song, W., Biswas, S., Suib, S.L., and He, J. (2015). Ligand-assisted co-assembly approach toward mesoporous hybrid catalysts of transition-metal oxides and noble metals: photochemical water splitting. Angew. Chem. Int. Ed. 127, 9189–9193.

43. Mohanty, P., Fei, Y., and Landskron, K. (2009). Synthesis of periodic mesoporous coesite. J. Am. Chem. Soc. 131, 9638–9639.

44. Wang, L., Wan, J., Zhao, Y., Yang, N., and Wang, D. (2019). Hollow multi-shelled structures of Co_3O_4 dodecahedron with unique crystal orientation for enhanced photocatalytic CO_2 reduction. J. Am. Chem. Soc. 141, 2238– 2241.

45. Liu, L., Jiang, Z., Fang, L., Xu, H., Zhang, H., Gu, X., and Wang, Y. (2017). Probing the crystal plane effect of Co_3O_4 for enhanced electrocatalytic

performance toward efficient overall water splitting. ACS Appl. Mater. Interfaces 9, 27736–27744.

46. Jin, Y., Wang, L., Shang, Y., Gao, J., Li, J., and He, X. (2015). Facile synthesis of monodisperse Co_3O_4 mesoporous microdisks as an anode material for lithium ion batteries. Electrochim. Acta 151, 109–117.

47. Xu, L., Jiang, Q., Xiao, Z., Li, X., Huo, J., Wang, S., and Dai, L. (2016). Plasma-engraved Co_3O_4 nanosheets with oxygen vacancies and high surface area for the oxygen evolution reaction. Angew. Chem. Int. Ed. 55, 5277–5281.

48. Wang, X., Zhuang, J., Peng, Q., and Li, Y. (2005). A general strategy for nanocrystal synthesis. Nature 437, 121–124.

49. Jiang, L., Sui, Y., Qi, J., Chang, Y., He, Y., Meng, Q., Wei, F., Sun, Z., and Jin, Y. (2017). Structure dependence of Fe-Co hydroxides on Fe/Co ratio and their application for supercapacitors. Part. Part. Syst. Charact. 34, 1600239.

50. Guan, J., Zhang, Z., Ji, J., Dou, M., and Wang, F. (2017). Hydrothermal synthesis of highly dispersed Co_3O_4 nanoparticles on biomassderived nitrogen-doped hierarchically porous carbon networks as an efficient bifunctional electrocatalyst for oxygen reduction and evolution reactions. ACS Appl. Mater. Interfaces 9, 30662–30669.

51. Song, W., Poyraz, A.S., Meng, Y., Ren, Z., Chen, S.-Y., and Suib, S.L. (2014). Mesoporous Co_3O_4 with controlled porosity: inverse micelle synthesis and high-performance catalytic CO oxidation at 60C. Chem. Mater. 26, 4629– 4639.

52. Dong, J., Song, L., Yin, J.-J., He, W., Wu, Y., Gu, N., and Zhang, Y. (2014). Co_3O_4 nanoparticles with multi-enzyme activities and their application in immunohistochemical assay. ACS Appl. Mater. Interfaces 6, 1959–1970.

53. Mu, J., Wang, Y., Zhao, M., and Zhang, L. (2012). Intrinsic peroxidase-like activity and catalase-like activity of Co_3O_4 nanoparticles. Chem. Commun. 48, 2540–2542.

54. Jin, L., Liu, B., Wu, Y., Thanneeru, S., and He, J. (2017). Synthesis of mesoporous CoS_2 and $Ni_xCo_{1-x}S_2$ with superior supercapacitive performance using a facile solid-phase sulfurization. ACS Appl. Mater. Interfaces 9, 36837–36848.

55. Plauck, A., Stangland, E.E., Dumesic, J.A., and Mavrikakis, M. (2016). Active sites and mechanisms for H_2O_2 decomposition over Pd catalysts. Proc. Natl. Acad. Sci. U S A 113, E1973–E1982.

56. Ford, D.C., Nilekar, A.U., Xu, Y., and Mavrikakis, M. (2010). Partial and complete reduction of O_2 by hydrogen on transition metal surfaces. Surf. Sci. 604, 1565–1575.

57. Marchesini, S., McGilvery, C.M., Bailey, J., and Petit, C. (2017). Template-free synthesis of highly porous boron nitride: insights into pore network design and impact on gas sorption. ACS Nano 11, 10003–10011.

58. Jiang, H.-L., Liu, B., Lan, Y.-Q., Kuratani, K., Akita, T., Shioyama, H., Zong, F., and Xu, Q. (2011). From metal-organic framework to nanoporous carbon: toward a very high surface area and hydrogen uptake. J. Am. Chem. Soc. 133, 11854–11857.

59. Kang, N., Park, J.H., Jin, M., Park, N., Lee, S.M., Kim, H.J., Kim, J.M., and Son, S.U. (2013). Microporous organic network hollow spheres: useful templates for nanoparticulate Co_3O_4 hollow oxidation catalysts. J. Am. Chem. Soc. 135, 19115–19118.